



# Institutional Repository - Research Portal

## Dépôt Institutionnel - Portail de la Recherche

[researchportal.unamur.be](https://researchportal.unamur.be)

## RESEARCH OUTPUTS / RÉSULTATS DE RECHERCHE

### **Electrochemical Investigation of Nitinol/Tantalum Hybrid Surfaces Modified by Alkylphosphonic Self-Assembled Monolayers**

Maho, Anthony; Kanoufi, Frédéric; Combellas, Catherine; Delhalle, Joseph; Mekhalif, Zineb

*Published in:*  
Electrochimica Acta

*DOI:*  
[10.1016/j.electacta.2013.11.008](https://doi.org/10.1016/j.electacta.2013.11.008)

*Publication date:*  
2014

*Document Version*  
Peer reviewed version

[Link to publication](#)

*Citation for pulished version (HARVARD):*

Maho, A, Kanoufi, F, Combellas, C, Delhalle, J & Mekhalif, Z 2014, 'Electrochemical Investigation of Nitinol/Tantalum Hybrid Surfaces Modified by Alkylphosphonic Self-Assembled Monolayers', *Electrochimica Acta*, vol. 116, pp. 78-88. <https://doi.org/10.1016/j.electacta.2013.11.008>

#### **General rights**

Copyright and moral rights for the publications made accessible in the public portal are retained by the authors and/or other copyright owners and it is a condition of accessing publications that users recognise and abide by the legal requirements associated with these rights.

- Users may download and print one copy of any publication from the public portal for the purpose of private study or research.
- You may not further distribute the material or use it for any profit-making activity or commercial gain
- You may freely distribute the URL identifying the publication in the public portal ?

#### **Take down policy**

If you believe that this document breaches copyright please contact us providing details, and we will remove access to the work immediately and investigate your claim.

# Electrochemical Investigation of Nitinol/Tantalum Hybrid Surfaces Modified by Alkylphosphonic Self-Assembled Monolayers

A. Maho<sup>a,b</sup>, F. Kanoufi<sup>c</sup>, C. Combellas<sup>c</sup>, J. Delhalle<sup>a</sup>, Z. Mekhalif<sup>a,\*</sup>

<sup>[a]</sup> Laboratory of Chemistry and Electrochemistry of Surfaces, University of Namur (FUNDP), Rue de Bruxelles 61, B-5000 Namur, Belgium.

<sup>[b]</sup> Fonds pour la Formation à la Recherche dans l'Industrie et dans l'Agriculture (FRIA), Rue d'Egmont 5, B-1000 Bruxelles, Belgium.

<sup>[c]</sup> Physico-Chimie des Electrolytes, des Colloïdes et Sciences Analytiques, ESPCI ParisTech, CNRS UMR 7195, Rue Vauquelin 10, 75231 Paris Cedex 05, France.

## Abstract

The surface characteristics of bare and modified nickel-titanium samples (NiTi) are investigated by spectroscopic, microscopic and electrochemical techniques. The successful electrodeposition of a tantalum coating on NiTi and the effective grafting of 1-dodecylphosphonic acid SAMs on both pristine and Ta-covered NiTi surfaces are evidenced and quantified by XPS and SEM. Cyclic voltammetry performed on the different NiTi-based electrodes highlights their specificities regarding electron transfer to a redox probe present in solution (here ruthenium(III) hexamine). Finally, the samples electrochemical characteristics at a local scale are investigated by scanning electrochemical microscopy (SECM). The impact of the surface modifications on mass transport of the redox probe is analyzed through approach curves in the feedback mode, while the recording of current maps in feedback as well as in substrate-generation/tip-collection modes leads to the qualitative identification of electrochemically-active areas corresponding to precursor pitting corrosion sites.

## Keywords

Nickel-titanium; tantalum electrodeposition; 1-dodecylphosphonic acid self-assembled monolayers; charge transfer; scanning electrochemical microscopy.

## Corresponding author

\* Prof. Zineb Mekhalif, Laboratory of Chemistry and Electrochemistry of Surfaces, University of Namur, Rue de Bruxelles 61, B-5000 Namur, Belgium. Tel.: +32 (0)81 72 52 30. Fax: +32 (0)81 72 46 00. E-mail: [zineb.mekhalif@unamur.be](mailto:zineb.mekhalif@unamur.be)

## 1. Introduction

The Nitinol alloy (NiTi, made of Ni and Ti in quasi equiatomic proportions) is well known for its excellent shape memory and superelasticity properties. It has captured attention as a basic material for usual and high technology devices, and also in the fields of medical instruments (surgical pliers, dental floss, endoscopes, ...) and implants (dental, orthopedic, cardiovascular, ...). In this framework, many researches are pursued towards the reduction of the immune response induced by the high nickel content, notably through the generation of a protective and biocompatible interface between the biomaterial and the human body [1-4]. The approach in several previous works consists of the elaboration on the NiTi surface of a thin tantalum (Ta) layer, a metal which is recognized for its excellent biocompatibility and bioactivity, its radio-opacity and its strong propensity to withstand corrosion processes [5-7]. Among the different chemical methodologies, which can be exploited for this purpose, electrodeposition in ionic liquids constitutes a technique of choice, notably for the control of the thickness of the prepared deposit and its highly accurate structuration [8-11]. A previous paper has highlighted and discussed the intrinsic nanoporous nature of the thin Ta deposit on the NiTi plates [11]. This hollowed morphology implies a possible contact between the extreme surface of the underlying NiTi substrate and the ambient atmosphere through the pores in the Ta film. In this perspective, a further modification of these surfaces by self-assembling of alkylphosphonic acid molecules, well known for their robust grafting on oxide-covered metals, has the potential to constitute a reinforced barrier layer against the aggressive environment. It also opens a wide range of interactions between the substrate and the external medium through a smart selection of the terminal functionality of the alkyl chain [12-17]. Such hybrid inorganic/organic surface films can thus create a fully protective layer on NiTi, but they are also acknowledged as beneficial contributors for a synergetic improvement of the global bioactivity of the platforms [9].

The recent study of the electrodeposition in an ionic liquid solution of a pristine Ta layer on NiTi plates was focusing on the chemical composition and the morphological features of these surfaces, mainly characterized through spectroscopic (X-ray photoelectron spectroscopy, XPS) and microscopic (scanning electron microscopy, SEM) techniques [11]. Another important fundamental consideration concerns the understanding and control of the electrochemical characteristics of such materials, especially with the perspective of evaluating their protective ability towards corrosion phenomena in biological environments. NiTi, as a platform material, has been the object of numerous related studies in the literature, whether as a native substrate, after surface treatment (polishing, heat treatment, ion implantation, ...) or modified by organic and inorganic coatings (self-assembled monolayers – SAMs –, metallic, ceramic or polymer films, ...) [2-4,16-26]. Most of the experimental characterizations concerning the corrosion resistance of the materials are pursued through polarization curves (or linear sweep voltammetry), cyclic voltammetry (CV) and electrochemical impedance spectroscopy, all of which focus on global scale observations. Developed during the late 80s by Bard's team, the scanning electrochemical

microscopy (SECM) technique has rapidly emerged as a highly promising and useful method to investigate the electrochemical and morphological characteristics of surfaces and interfaces at a more local scale (typically micrometric). Many topics are still investigated through SECM experiments, from classical surface technologies (SAMs, polymer coatings, membranes, nanostructures, electrodes, fuel cells, ...) to biological and medical fields (sensors, enzymes, living cells and tissues, DNA, ...) [27-32]. SECM can also be considered as a valuable tool for the local electrochemical characterization of thin passive oxide(s) layers covering numbers of metals and alloys. Several research groups have focused their interest on the behavior of the oxide films covering substrates such as Ti and alloys [33-41], Ta [42,43], Al [44], Fe and alloys [44,45], Zn [45], Ni [46], Cu [47], ITO [48], etc. Among them, White and co-workers specifically managed to highlight the presence of characteristic “electrochemically-active areas” on different surfaces – notably  $\text{TiO}_2$  and  $\text{Ta}_2\text{O}_5$  – corresponding to pitting [corrosion] precursor sites [33-37,42,43]. Those studies can thus be considered here in the perspective of investigating metallic electrodeposits and/or SAMs on solid surfaces, and more precisely for the characterization of titanium- and tantalum-based substrates.

Here, XPS, SEM, CV and SECM characterization techniques are used to evaluate the proper structural features of NiTi-based electrodes and assess their relative behavior towards electrochemical processes with reactive species in solution, notably in the framework of corrosion phenomena. Specifically, bare NiTi samples as well as substrates modified by tantalum and phosphonic acids (separately or additionally) are considered hereafter.

## 2. Experimental

### 2.1. Products and reagents

The following chemicals and solvents are handled without further purification for the pretreatment of the NiTi substrates and for the electrodeposition process of tantalum: absolute ethanol (VWR Prolabo), acetone (Chem-Lab, 99+%), ultra-pure water (18.2 MΩ cm), 1-butyl-1-methylpyrrolidinium bis(trifluoromethylsulfonyl)imide ionic liquid (99%), tantalum fluoride (Aldrich, 98%), lithium fluoride (Sigma-Aldrich, ≥99%). For the organic modification of the substrates, 1-dodecylphosphonic acid (95%) is supplied by Alfa Aesar. Products used for the electrochemical characterizations are ruthenium(III) hexamine trichloride (Aldrich, 98%) and potassium sulfate (Acros, 99+%).

### 2.2. Nitinol substrates preparation

NiTi rectangular coupons (20 x 10 x 0.3 mm<sup>3</sup>), purchased from AMF, are constituted of Ni (56%) and Ti (balance). They are first mechanically polished on a Buehler-Phoenix 4000 instrument using silicon carbide papers (P800, then P1200) and diamond pastes (9, 3, then 1 μm) from Struers. The NiTi plates are then cleaned in absolute ethanol under ultrasonication

for 15 min, submitted to UV-ozone for 30 min (Jelight 42-220), and finally ultrasonically treated in absolute ethanol for 15 other min, before being blown dry under nitrogen and stored for further use or analysis (Fig. 1a).

### 2.3. Tantalum electrodeposition on NiTi substrates.

The covering of the pretreated NiTi samples by an electrodeposited tantalum layer is performed in an argon-filled glove box (residual quantities of water and oxygen below 30 ppm) with an EG&G Princeton Applied Research, Potentiostat/Galvanostat Model 263A. The electrolytic solution is constituted of 0.10 M  $\text{TaF}_5$  and 0.25 M LiF in the 1-butyl-1-methylpyrrolidinium bis(trifluoromethylsulfonyl)imide ionic liquid ((BMP) $\text{Tf}_2\text{N}$ ). The electrodeposition of Ta is processed under galvanostatic conditions at ambient temperature (25°C): a constant current of  $-100 \mu\text{A}/\text{cm}^2$  is applied to the NiTi working electrode for 1 h versus a platinum foil acting as both reference and auxiliary electrodes. The modified samples are further post-treated by copious rinsing with acetone, immersed for 15 min in boiling water, then for 15 min in absolute ethanol under ultrasonication, blown dry under nitrogen and finally submitted to UV-ozone for 15 min (Fig. 1b) [9-11].

### 2.4. Self-assembling of 1-dodecylphosphonic acid

Organic modification of both pretreated NiTi (Fig. 1c) and Ta-covered NiTi (Fig. 1d) substrates is performed through their immersion in 10 mL of a 1 mM solution of 1-dodecylphosphonic acid ( $\text{C}_{12}\text{P}$ ) in absolute ethanol for 24 h at ambient temperature. The samples are then copiously rinsed with absolute ethanol, blown dry under nitrogen and stored until analysis.

### 2.5. XPS characterization

XPS is used to assess the presence of the Ta electrodeposit and/or the  $\text{C}_{12}\text{P}$  monolayer on the NiTi substrates, and to qualitatively and quantitatively check the composition of the different surfaces. Spectra are recorded on a Thermo Scientific K-Alpha spectrometer and treated using the Thermo Advantage v5.27 software. The photoelectrons are excited using a monochromatic Al  $\text{K}\alpha$  radiation as the excitation source, collected at  $\theta = 0^\circ$  with respect to the surface normal and detected with a hemispherical analyzer. The spot size of the XPS source on the sample is 200  $\mu\text{m}$ , and the analyzer is operated with a pass energy of 150 eV for survey spectra and 20 eV for accumulation spectra on core levels. Pressure is kept below  $1 \times 10^{-8}$  Torr during data collection and the binding energies ( $E_b$ ) of the obtained peaks are referenced to the C1s signal for C-H, set at 285.0 eV. Spectra are fitted using a Smart background and a linear combination of Gaussian and Lorentzian profiles in 70-30 proportions. Peak positions obtained after analysis are found essentially constant ( $\pm 0.3$  eV). The different relative peak intensities and areas are finally measured on core levels spectra. Sensitivity factors used for the different atoms are: C1s 1.000, O1s 2.930, Ni2p 22.180, Ti2p<sub>1/2</sub> 2.690, Ti2p<sub>3/2</sub> 5.220, Ta4f<sub>5/2</sub> 3.800, Ta4f<sub>7/2</sub> 4.820, F1s 4.430, and P2p 1.192. Thickness

and coverage values for tantalum and alkylphosphonic coatings are estimated from the collected XPS data. In all generality, the thickness of a layer material *A* deposited on a bulk material *B* can be obtained from the relative attenuation of the *B* element signal, which is quantified as:

$$\frac{I_B}{I_{B,0}} = \exp\left(-\frac{d_A}{\lambda_{B,A}} \sin \theta\right) \quad (1)$$

where  $I_B/I_{B,0}$  is the ratio of the bulk element *B* peak intensities (modified surface/bare surface),  $d_A$  the layer material *A* thickness,  $\lambda_{B,A}$  the bulk material *B* photoelectrons mean free path through layer material *A*, and  $\theta$  the takeoff angle (here  $\theta = 0^\circ$ ) [49,50].

## 2.6. SEM imaging

A JEOL 7500F scanning electron microscope is used to image the morphological and structural features of the NiTi-based surfaces.

## 2.7. Electrochemical analyses

### 2.7.1. Cyclic voltammetry

Prior to the SECM characterizations, the potential of the different NiTi substrates (pristine and modified with Ta and/or  $C_{12}P$  SAMs) is scanned at a rate of 20 mV/s within the -0.8/+0.5 V/Ag-AgCl potential window, starting from 0 V/Ag-AgCl with a negative initial scan polarity. The obtained voltammograms provide a direct qualitative and quantitative assessment of the blocking effect of the Ta electrodeposit and/or the  $C_{12}P$  monolayer present on NiTi on the electron transfer from the sample to  $Ru(NH_3)_6^{3+}$ . Briefly, the quantitative CV analysis consists of extracting the apparent electron transfer rate constant,  $k_{app}^\circ$ , from the voltammogram, which is done using semi-deconvolution analysis of the curves. For a quasi-reversible process, the variation of the electron transfer rate  $k$  with the potential  $E$  is given from the current  $i(E)$  by:

$$k(E) = \frac{i(E)\sqrt{D}}{I_{lim} - I(E) \left(1 + \exp\left(-\frac{nF}{RT}(E - E^0)\right)\right)} \quad (2)$$

where  $I_{lim}$  is the diffusion limiting current of the sigmoidal convoluted current  $I(E)$ , and  $D$  the probe diffusion coefficient ( $D = 7.4 \times 10^{-6} \text{ cm}^2/\text{s}$  for  $Ru(NH_3)_6Cl_3$  [40]). The extrapolation of  $k(E)$  to  $E = E^0$  leads to  $k_{app}^\circ$ , with the  $E^0$  value being estimated to -0.19 V/Ag-AgCl from the electrochemical response of an inert Pt electrode. This strategy allows for a pertinent estimate of  $k_{app}^\circ$  for peak-shaped voltammograms without a precise knowledge of the electrode surface area [31,32,51,52].

### 2.7.2. SECM in the Feedback (FB) mode: approach curves and imaging.

SECM is achieved with a CHI 900B (CH Instruments), using a three-electrode cell with a commercial Ag-AgCl reference electrode (CH Instruments, CHI111), a platinum wire as counter electrode, and a 10  $\mu\text{m}$  diameter platinum microdisc ultramicroelectrode (UME), with an estimated RG ratio of 15, as the first working electrode (CH Instruments, CHI107). The NiTi-based sample is fixed to the bottom of the Teflon cell and acts as the second working electrode. Both potentials of the UME tip and the analyzed substrate can be controlled independently using a bipotentiostat. The working solution is composed of 5 mM  $\text{Ru}(\text{NH}_3)_6\text{Cl}_3$  as the redox mediator and 0.1 M  $\text{K}_2\text{SO}_4$  as the supporting electrolyte, in ultra-pure water.

Analyses in the FB mode are completed in a 5 mM  $\text{Ru}(\text{NH}_3)_6\text{Cl}_3$  / 0.1 M  $\text{K}_2\text{SO}_4$  working solution according to the following scheme. First, the tip is moved down to the substrate at a rate of 2  $\mu\text{m/s}$ , and an approach curve is recorded: the UME is polarized ( $E_{\text{tip}}$ ) to -0.70 V/Ag-AgCl (to allow for the mass-transfer controlled reduction of  $\text{Ru}(\text{NH}_3)_6^{3+}$  into  $\text{Ru}(\text{NH}_3)_6^{2+}$ ), and the substrate ( $E_{\text{substrate}}$ ) is left at open circuit potential (OCP). The approach is stopped when a sharp change of the current occurs at the tip, as a result of a contact between the UME and the substrate surface ( $d = 0$ ). The UME is then withdrawn by 10  $\mu\text{m}$ , and the SECM FB imaging is carried out by scanning a 300 x 300  $\mu\text{m}^2$  area at a x,y-scan rate of 25  $\mu\text{m/s}$ . During the whole duration of the imaging process, the substrate is kept at OCP while the tip remains polarized at  $E_{\text{tip}} = -0.70$  V/Ag-AgCl.

### 2.7.3. SECM in the Substrate-Generation/Tip-Collection (SG-TC) mode: imaging

SECM maps obtained in the SG-TC mode are performed according to a similar procedure. First, a typical approach curve is obtained in the FB mode ( $E_{\text{tip}} = -0.70$  V,  $E_{\text{substrate}} = \text{OCP}$ ) in order to correctly position the tip, which is then removed of 10  $\mu\text{m}$  from the substrate surface. At this point, the NiTi-based sample is polarized via the bipotentiostat at a value that allows for the conversion of  $\text{Ru}(\text{NH}_3)_6^{3+}$  into  $\text{Ru}(\text{NH}_3)_6^{2+}$  in electrochemically-active sites or regions. This value of  $E_{\text{substrate}}$  is determined from the corresponding voltammogram initially measured (Section 2.7.1.).  $E_{\text{tip}}$  is set at +0.10 V/Ag-AgCl in order to collect the  $\text{Ru}(\text{NH}_3)_6^{2+}$  entities and convert them back into their initial  $\text{Ru}(\text{NH}_3)_6^{3+}$  form. SECM SG-TC imaging is then proceeded on 300 x 300  $\mu\text{m}^2$  areas at a x,y-scan rate of 25  $\mu\text{m/s}$ .

## 3. Results and discussion

### 3.1. XPS

The qualitative and quantitative evaluation of the surface atomic composition of the different substrates is carried out by XPS. In particular, the tantalum covering rate after the electrodeposition and/or the quality of the grafting of 1-dodecylphosphonic acid monolayers, as well as the thickness of the two deposited layers, are assessed prior to any further characterization.

Survey spectra of NiTi, NiTi-C<sub>12</sub>P, NiTi-Ta and NiTi-Ta-C<sub>12</sub>P are shown in Fig. 2 (a, b, c and d, respectively). Ni2p and Ti2p signals are present in each case, indicating the accessibility of NiTi underlayer to photoelectrons for all substrates. The grafting of the C<sub>12</sub>P SAM is confirmed on NiTi-C<sub>12</sub>P and NiTi-Ta-C<sub>12</sub>P by a significant increase of the C1s peak intensity and the P2s and P2p signals (inserts on Fig. 2b and 2d), compared to the pristine NiTi sample. The characteristic core levels of Ta (notably Ta4p, Ta4d and Ta4f) are found on the NiTi-Ta and NiTi-Ta-C<sub>12</sub>P spectra, proof of the electrodeposit on NiTi. A very slight residual fluorine contamination (F1s signal), coming from chemical species contained in the electrodeposition bath, is also noticed for the latter two substrates.

Table 1 reports the different elemental percentages and atomic ratios measured on the four samples. Interestingly, the ratio of Ti and Ni is evolving from a Ti majority on bare NiTi to a Ni excess after Ta modification. As mentioned in a previous study [11], this reversal can be explained as a consequence of the Ta electrodeposition process. The F<sup>-</sup> ions contained in the electrolytic solution (made of TaF<sub>5</sub> and LiF) allow for the partial abrasion of Ni entities present at the extreme surface. As this phenomenon occurs concurrently with the electrodeposition of Ta, a certain amount of nickel-containing species is trapped between the NiTi platform and the Ta layer in formation, which results in a larger quantity of Ni detected by XPS [11]. Regarding the grafting of the C<sub>12</sub>P SAMs, its efficiency is confirmed out of the C1s/P2p ratios for the NiTi-C<sub>12</sub>P and NiTi-Ta-C<sub>12</sub>P samples, since the experimental values (13 and 14, respectively) stand quite close to the theoretical one ( $C1s/P2p_{theor} = 12$ ). The slight difference is due to the presence of few carbon contaminants inherent to the experimental protocol. These first XPS results highlight the presence of good quality Ta electrodeposits and/or C<sub>12</sub>P SAMs on the NiTi samples.

Conceptual equations, based on the mean free path of the substrate-specific photoelectrons, have been proposed through the literature to estimate surface films thickness and coverage ratio, notably for oxide native overlayers and nanometric organic adlayers present on specific metallic substrates [49,50,53-57]. We propose here to conceptualize the present experimental substrates NiTi-C<sub>12</sub>P and NiTi-Ta as simple cases of an overlayer of material/element *A* on a substrate of material/element *B*. The thickness of the different layers is then calculated from the attenuation of the *B* material/element signal after the surface modification, according to Eq. (1). Since the Nitinol extreme surface is mainly constituted of titanium dioxide [53], the Ti2p signal is considered here for the quantification of the substrate photoelectrons attenuation after their passage through the phosphonic or tantalum layer. For NiTi-Ta-C<sub>12</sub>P samples, the decrease of the Ta4f peak intensity (in the Ta<sub>2</sub>O<sub>5</sub> form) after the C<sub>12</sub>P treatment is examined for the calculation of the SAM thickness. Photoelectron escape depth numeric values have been established from the works of Cumpson and Seah by assimilating the C<sub>12</sub>P layer to a pure carbon matrix (density = 1.0 g/cm<sup>3</sup>) and the Ta deposit to a pure and homogeneous Ta<sub>2</sub>O<sub>5</sub> film (density = 8.2 g/cm<sup>3</sup>) [49].



Peak intensity, mean free path and calculated thickness values are reported in Table 2. By applying Eq. (1) to the Ti2p peak intensities recorded on both NiTi (bare substrate,  $I_{B,0}$ ) and NiTi-C<sub>12</sub>P (modified substrate,  $I_B$ ) core level spectra (Fig. 3a), an average thickness value of 0.8 nm is obtained for the C<sub>12</sub>P layers on NiTi. In a similar way, the Ta4f signal (Fig. 3b) inhibition is used to determine a thickness of 0.7 nm for the C<sub>12</sub>P films on Ta-covered NiTi (with NiTi-Ta and NiTi-Ta-C<sub>12</sub>P acting here as bare and modified substrates, respectively). Both thicknesses are of the same order. As the C<sub>12</sub>P molecule size equals approximately 1.2 nm, we can reckon a covering ratio by C<sub>12</sub>P of ~ 60% on both bare and Ta-modified NiTi. The analysis is also made with Ti2p core levels on NiTi and NiTi-Ta samples (Fig. 3c), and results in a 2.1 nm thickness for the Ta<sub>2</sub>O<sub>5</sub> deposit on NiTi. With a  $I_{TiO_2}/I_{TiO_2,0}$  value of 0.15 and a layer thickness (2.1 nm) being inferior to the experimental mean free path (4.5 nm), we can postulate a coverage by Ta<sub>2</sub>O<sub>5</sub> on NiTi of ~ 85%.

This being said, the discussion and exploitation of those experimental thickness and covering rate values should be carried on with very deep caution due to the relative complexity of the presently considered interfaces, being atomically unsmooth and constituted of various forms of nickel-titanium surface oxides and hydroxides, porous-nanostructured Ta<sub>2</sub>O<sub>5</sub> electrodeposits and/or phosphonic acid monolayers. These results should thus be preferably regarded as a relatively rough estimate of experimental trends obtained from modeled thin interfaces. In this perspective, the electrochemical studies described in the following sections are well indicated to address those issues and achieve a more documented and complete discussion.

### 3.2. Cyclic voltammetry

Fig. 4 presents the voltammograms of pristine and modified NiTi samples recorded in a 5 mM Ru(NH<sub>3</sub>)<sub>6</sub>Cl<sub>3</sub> / 0.1 M K<sub>2</sub>SO<sub>4</sub> solution, at a scan rate  $v$  of 20 mV/s. All substrates exhibit the characteristic voltammogram of the Ru(NH<sub>3</sub>)<sub>6</sub><sup>3+</sup> / Ru(NH<sub>3</sub>)<sub>6</sub><sup>2+</sup> mediator system. The same curves measured in “blank” solutions – containing only 0.1 M K<sub>2</sub>SO<sub>4</sub> – display no characteristic signal, which attests that only the electron transfer reaction at the mediator is occurring. Compared to the electrochemical response of an inert Pt electrode, only the backward sweep showing the oxidation of electrogenerated Ru(NH<sub>3</sub>)<sub>6</sub><sup>2+</sup> at  $E_{\text{substrate}} > -0.2$  V/Ag-AgCl is of poor quality. It may result from the oxidized form of the NiTi and NiTi-Ta surfaces, most of the investigated surfaces being composed of TiO<sub>2</sub> or Ta<sub>2</sub>O<sub>5</sub> (cf. XPS analyses in section 3.1). As already proposed for Ta/Ta<sub>2</sub>O<sub>5</sub> surfaces [42], the incomplete reoxidation of Ru(NH<sub>3</sub>)<sub>6</sub><sup>2+</sup> at these large band-gap n-type semiconductors could be indicative of the position of their conduction band edge,  $E_{cb}$ , which would be more negative than the formal potential  $E^0$  of Ru(NH<sub>3</sub>)<sub>6</sub><sup>3+/2+</sup>. In the following, we thus consider specifically the cathodic peak on the forward scan of the four samples, and significant differences are noticed at this level from one substrate to another (Table 3). In terms of current values, pristine NiTi and NiTi-Ta exhibit intense peak currents  $i_p$  of -0.146 and -0.126 mA (respectively) while those of NiTi-C<sub>12</sub>P and NiTi-Ta-C<sub>12</sub>P decrease down to -0.060 and -0.067 mA (respectively), which seems

closely related to the presence of the C<sub>12</sub>P SAM. Considering the peak potentials,  $E_p$ , they are rather shifted towards more cathodic values when the tantalum electrodeposit is present: samples without Ta – NiTi and NiTi-C<sub>12</sub>P – present peak potentials of -0.34 and -0.31 V (respectively), while values for samples with Ta – NiTi-Ta and NiTi-Ta-C<sub>12</sub>P – are -0.45 and -0.44 V (respectively). From these observations, a Tafel analysis of the CVs gives access to apparent standard electron transfer rate constants,  $k_{app}^\circ$  [31,32,51,52]. A clear distinction appears between the effects of a covering by tantalum or by phosphonic acid molecules: the electrodeposition of Ta considerably decreases the corresponding values of  $k_{app}^\circ$  (from  $3.1 \times 10^{-4}$  to  $0.92 \times 10^{-4}$  cm/s between NiTi and NiTi-Ta; from  $2.9 \times 10^{-4}$  to  $0.87 \times 10^{-4}$  cm/s between NiTi-C<sub>12</sub>P and NiTi-Ta-C<sub>12</sub>P), while the grafting of a C<sub>12</sub>P monolayer has no significant effect ( $3.1$  and  $2.9 \times 10^{-4}$  cm/s for NiTi and NiTi-C<sub>12</sub>P,  $0.92$  and  $0.87 \times 10^{-4}$  cm/s for NiTi-Ta and NiTi-Ta-C<sub>12</sub>P).

Analogies can be established at this stage with model electrode surfaces partially covered by a coating, which blocks the electron transfer to the redox probe in solution. Within such model framework, electron transfer occurring on coated electrodes results from charge transfer within the imperfections or defects of the film. The observed electrochemical response can then be used to describe the size and density of the defects within the coating. Complete theoretical descriptions of such an issue have been proposed for various defects size, density, shape and distribution [52,58,59]. Briefly, small and sparse defects behave as independent micro/nanoelectrodes and the CV presents a steady-state sigmoidal response, while in the case of more dense networks, the interpenetration of the diffusion layers of each defect may occur and the peak-diffusion shape of the CV is restored [52,58]. Different situations can then arise, depending on the size of the defects. “Macroscopic” defects (of dimension  $> \mu\text{m}$ ) result in the decrease of the peak current as an apparent decrease of the active part of the electrode [59]. For “microscopic” defects, with a sub-micrometric size, the diffusion-peak-shaped intensity is the same as that of the uncovered electrode, the electrode coverage then results in the apparent decrease of the electron transfer kinetics compared to the uncovered one [52]. Qualitatively, these situations fit the experimental situations observed here and the C<sub>12</sub>P layer would form “macroscopic” defects while the Ta layer “microscopic” ones. We then use the proposed models to depict the different kinds of coverage of NiTi electrodes.

First, it has already been shown that such a Ta electrodeposit on NiTi presented regular disk-shape nanometric pores, with an average diameter of 120 nm and an average edge-to-edge distance of 150 nm [11]. A SEM image of the dimpled layer is shown in Fig. 5. This configuration corresponds to the “microscopic” defects described in Amatore’s model [52]. The partial blocking of the NiTi electrode surface by the Ta electrodeposit should then correspond to a decrease of the standard rate constant  $k_{app}^\circ$  proportionally to the covering rate  $\vartheta_{Ta}$  of the sample by Ta, following the relation [52]:

$$k_{app}^\circ(\text{NiTi-Ta}) = k_{app}^\circ(\text{NiTi}) \times (1 - \vartheta_{Ta}) \quad (3)$$

where  $k_{app}^{\circ}(M)$  corresponds to the apparent electron transfer rate constant estimated at the electrode M from semi-deconvolution of the CV (Section 2.7.1.) [31,32,51,52]. Then, a covering rate,  $\vartheta_{Ta}$ , of  $\sim 70\%$  is deduced from the experimental  $k_{app}^{\circ}$  values, where  $\sim 85\%$  was obtained from XPS quantification and  $\sim 50\%$  from SEM views (Fig. 5) [11]. The model also states that, in ideal situations, the peak currents are not affected by the blocking of the electrode surface, which is observed here with values of  $-0.146$  and  $-0.126$  mA for NiTi and NiTi-Ta, respectively. The small current decrease observed after the coverage of NiTi by Ta actually corresponds to the theoretical peak current decrease associated to the decrease of ET reversibility (decrease of  $k_{app}^{\circ}$ ) when going from NiTi to NiTi-Ta.

At a scan rate of  $100$  mV/s (not shown), the CV still shows a diffusive peak-shape. It signifies that at this time range, the nanopores in the Ta layer behave as an array of interpenetrating nanoelectrodes characterized by a linear diffusion. This indicates that the characteristic diffusion length explored by CV,  $\delta = (DRT/Fv)^{1/2}$  (with  $D$  the redox probe diffusivity, estimated to  $7.4 \times 10^{-6}$  cm<sup>2</sup>/s for  $Ru(NH_3)_6Cl_3$  [40]), approximately  $15$   $\mu$ m, is more than  $100$  times larger than the average edge-to-edge length between two nanopores,  $R_0$ . Indeed, according to the kinetic zone diagram presented in ref. [52], deviation from diffusion peak-shape voltammogram to sigmoidal steady-state one occurs for  $\delta < 100 R_0$ . This observation fits with the general SEM picture (Fig. 5) where  $R_0 = 150$  nm [11]. As the morphological nature of the Ta layer is known to be dependent on the electrodeposition duration [11], it would be of interest to further check and discuss the evolution of the ET reversibility and  $k_{app}^{\circ}$  for thicker, denser and pores-filled Ta deposits obtained after longer preparation times (work in progress).

Concerning the surface modification with a  $C_{12}P$  SAM, the model of Matsuda *et al.*, concerning electrode surfaces with “macroscopic” inhomogeneities, is applicable here [59]. According to this model, the coverage of NiTi by the  $C_{12}P$  monolayer should not affect the electron transfer kinetics between the substrate and  $Ru(NH_3)_6^{3+}/Ru(NH_3)_6^{2+}$  ions present in the solution ( $k_{app}^{\circ}$ ). Only the current density parameter should vary from unmodified to modified samples proportionally to the uncovered portion of the electrode: the higher the covering rate by  $C_{12}P$  ( $\vartheta_{C12P}$ ), the more important the decrease of the current peak intensity. From the experimental values of charge densities  $Q$ , the  $\vartheta_{C12P}$  values for NiTi- $C_{12}P$  and NiTi-Ta- $C_{12}P$  are estimated to  $68$  and  $41\%$  (respectively), according to:

$$\vartheta_{C12P}(NiTi-C_{12}P) = (Q_{NiTi} - Q_{NiTi-C12P}) / Q_{NiTi} \quad (4)$$

$$\vartheta_{C12P}(NiTi-Ta-C_{12}P) = (Q_{NiTi-Ta} - Q_{NiTi-Ta-C12P}) / Q_{NiTi-Ta} \quad (5)$$

Those values obviously evidence that the  $C_{12}P$  SAM is not fully covering the surface of the pristine NiTi and NiTi-Ta samples. In the case of NiTi surface the coverage is in good agreement with that obtained from XPS. In the case of the NiTi-Ta sample, already covered with a blocking layer of Ta, it has been shown that the electrode behaves as an array of interpenetrating nanoelectrodes. The surface coverage of  $41\%$  obtained in Eq. (5) should

correspond to the coverage of the electroactive part of the array of nanopores, that is Ta-uncovered NiTi. From CV analysis, no indication on the coverage of the Ta layer by C<sub>12</sub>P is obtained. However, it is clear from XPS analysis that C<sub>12</sub>P molecules are also present onto the Ta layer (Fig. 2 and Table 1), and that the coverage by C<sub>12</sub>P is equivalent as well on bare as on Ta-modified NiTi (globally 60%, out of XPS quantification, Fig. 3 and Table 2). The incomplete coverage of the surfaces by C<sub>12</sub>P, with “macroscopic” defects, is probably related to the experimental conditions selected for the grafting of the C<sub>12</sub>P film on the substrates. Indeed, many studies have already discussed the crucial importance of parameters such as solvent, temperature, time, pH, and alkyl chain length for the preparation of dense and well-organized phosphonic acid monolayers [14,17,60-63]. The conditions defined here correspond to a pragmatic grafting of the C<sub>12</sub>P molecules in the perspective of developing prototype interfaces for advanced experimental protocols of electrochemical analyses on NiTi-based substrates.

### 3.3. SECM

The different surface modifications on NiTi samples were first investigated in the FB mode. By comparison with the CV inspection, the mass transport of the Ru(NH<sub>3</sub>)<sub>6</sub><sup>2+</sup> tip-generated redox probe between the surface, the bulk solution and the Pt UME is investigated through FB approach curves. Recording of SECM FB and SG/TC images of the surfaces in solution of Ru(NH<sub>3</sub>)<sub>6</sub><sup>3+</sup> is then carried out and commented.

#### 3.3.1. FB approach curves

Normalized approach curves (normalized current  $i_T/i_{T,0}$  vs. normalized tip position  $d/r_T$ ) recorded in the FB mode are displayed in Fig. 6. The curves are fitted by general analytical expressions given for first-order heterogeneous finite kinetics at the sample surface with respect to the Ru(NH<sub>3</sub>)<sub>6</sub><sup>2+</sup> species electrogenerated at the tip. The fitting procedure consists of comparing the experimental approach curves to analytical expressions [64,65] in order to determine the apparent charge transfer rate constants,  $k_{eff}$ , describing the rate of regeneration of Ru(NH<sub>3</sub>)<sub>6</sub><sup>3+</sup> by the substrate. An increasing hindered diffusion of the mediator is observed and quantified from NiTi ( $k_{eff} = 4.6 \times 10^{-3}$  cm/s) to NiTi-Ta-C<sub>12</sub>P ( $1.1 \times 10^{-3}$  cm/s), with NiTi-C<sub>12</sub>P ( $1.9 \times 10^{-3}$  cm/s) and NiTi-Ta ( $1.7 \times 10^{-3}$  cm/s) standing close to each other in an intermediary situation (Table 4). Those values point out that the combination of a Ta electrodeposit with a C<sub>12</sub>P monolayer induces a sizeable blocking effect on the mass transfer processes of the mediator all over the surface. Taken separately, the Ta and SAM modifications increase the trend compared to a pristine NiTi substrate, but slightly less than when they are both achieved.

Absolute and relative values obtained for  $k_{eff}$  after fitting the experimental approach curves (Fig. 6 and Table 4) do not directly correspond to their  $k_{app}^\circ$  counterparts calculated out of cyclic voltammograms (Fig. 4 and Table 3). In ideal cases,  $k_{eff}$  constants measured by SECM approach curves in the FB mode state for the regeneration of the mediator (Ru(NH<sub>3</sub>)<sub>6</sub><sup>3+</sup> ↔

$\text{Ru}(\text{NH}_3)_6^{2+}$ ) only limited by mass transfers between the substrate surface, the bulk solution and the UME tip, while  $k_{app}^\circ$  determined out CV curves express a kinetic limitation effect by the electron transfer. To correctly correlate both data sets, the comparison must concern the experimental ratios of SECM first-order heterogeneous kinetics rate constants,  $k_{eff}$ , and peak current intensities,  $i_p$ , measured on voltammograms, reflecting mass-transfer controlled processes (Tables 3 and 4). But the CVs examine the reductive process of the redox probe while the approach curves rather check the oxidative process, which makes the comparison difficult, owing to the poor quality of the backward oxidative scan. This probably results from the passivation of the NiTi-based electrode in this potential range, which does not lead to a current response of good quality. However, interesting changes in the mass transfer regime have been detected from CV as the  $\text{C}_{12}\text{P}$  grafting yielded the apparent decrease of the electrode surface area due to the presence of “macroscopic” defects. The SECM approach curves should also detect such variations and the decrease in  $k_{eff}$  observed upon  $\text{C}_{12}\text{P}$  grafting should follow the one observed in the peak currents decrease. The correspondence is indeed well noted for NiTi and NiTi- $\text{C}_{12}\text{P}$  samples (ratios values of 2.5 for  $k_{eff}$  and 2.4 for  $i_p$ ), and to a lesser extent for NiTi-Ta and NiTi-Ta- $\text{C}_{12}\text{P}$  (1.5 for  $k_{eff}$  vs. 1.9 for  $i_p$ ).

A NiTi sample covered with a Ta electrodeposit also presents an interesting surface as it was shown to behave as an array of nanoelectrodes (Section 3.2.). It is expected that the mass-transfer limited flux emitted by such arrays is characterized by an apparent mass-transfer rate  $k_{eff,lim} = 4NRD$  with  $D$  the redox probe diffusivity,  $R$  the nanoelectrodes average radius and  $N$  their density within the array. The SEM inspection suggests  $k_{eff,lim} = 0.80 \text{ cm/s}$  (obtained with  $D = 7.4 \times 10^{-6} \text{ cm}^2/\text{s}$ ,  $R = 60 \text{ nm}$  and  $N = 4.5 \times 10^9 \text{ pores}/\text{cm}^2$ ) [11], which is much higher than the experimental determination from the FB approach curves ( $1.7 \times 10^{-3} \text{ cm/s}$ ). Actually, the nanoelectrodes formed by the nanoporous Ta film were shown not to behave as independent sources but to present overlapping diffusion layers. The mass transfer rate for such array is then expected to be much lower than  $k_{eff,lim}$ . Similar conclusion about overlapping diffusion layer from nanosources was actually pointed out by Nugues and Denuault in the investigation of charge transfer across porous membranes [66].

The qualitative and quantitative study of the different SECM approach curves, as well as the cyclic voltammograms discussed above, highlights thus the local characteristics of NiTi-based materials in terms of electrochemical and electronic phenomena: the NiTi functionalization by Ta and/or  $\text{C}_{12}\text{P}$  layers induces the progressive reinforcement of the blocking effect on electron transfers at the surfaces. In further applied perspectives, these observations must be considered with attention knowing the fundamental importance of heterogeneous electron-transfer reactions that occur between a metallic biomaterial and the adsorbed proteins naturally covering it when implanted in the human body [67].

### 3.3.2. Imaging: FB vs. SG/TC modes

After the collection of the FB approach curves for the different substrates, we have recorded corresponding SECM FB maps of the surfaces. For the sake of straightforwardness, only the

NiTi-Ta-C<sub>12</sub>P case (with full surface modification) will be developed further here, the three other samples leading to similar observations. As observed in Fig. 7, the image resolution is very poor in the FB mode and does not allow for the obvious observation of any morphological special feature. This is not surprising considering the structure of the surfaces: nanopores in the Ta layer are too small ( $\varnothing \sim 150$  nm) to be imaged by the microelectrode, and the covering by the C<sub>12</sub>P SAM does not sufficiently impact the current parameter to reveal the “macroscopic” defects assumed from the CV analysis. This points out that, with NiTi-based samples, SECM FB imaging on a substrate left at OCP cannot lead to well-defined maps of the different surfaces. This could result from the redox conversion of the selected mediator and the resulting electron and mass transfers with the surface and the tip are not sufficiently “fueled”, mainly because of too passive FB conditions. Indeed, working with a substrate at OCP involves electronic transfers with a zero or weak driving force from the substrate. Moreover, as the NiTi samples respond more efficiently under cathodic conditions (as seen by comparing oxidative and reductive peaks in Fig. 4), attempts to “activate” the imaging of the charge transfer process via the polarization of the NiTi-based sample has been pursued through the SG-TC operation mode.

A representative SECM image in the SG-TC mode of NiTi-Ta-C<sub>12</sub>P surfaces is reported in Fig. 8. It is important to specify at this stage that the scan is recorded at the exact same x,y,z-location as its corresponding FB counterpart presented in Fig. 7, the only change between both representations being the applied  $E_{tip}$  and  $E_{substrate}$ . In this way, a direct comparison between SECM imaging of NiTi-based substrates in FB and SG-TC modes can be discussed. The selection of the  $E_{substrate}$  value in SG-TC mode is based on the voltammetry curves of the samples (Fig. 4, Table 3). For Ti, as well as for Ta-based surfaces, White *et al.* have shown that the apparent electrochemical activity of surface pitting precursor sites correlates very well with the magnitude of the faradic current measured in the voltammograms, and thus that the SECM image contrast is directly dependent on the potential applied to the sample [33-37,42,43]. From the observations in Fig. 4, a maximal resolution for the observation of electrochemically-active sites by SECM imaging in SG-TC mode will be obtained by applying a  $E_{substrate}$  value corresponding to the peak potential of the substrate (Table 3). Thus a potential of -0.44 V/Ag-AgCl is considered for NiTi-Ta-C<sub>12</sub>P (Fig. 8),  $E_{tip}$  being kept at +0.10 V/Ag-AgCl in all cases.

The first issue concerns the global resolution of the image, which is substantially improved with SG-TC compared to FB. Short-range variations of the electrochemical activity are now clearly observable. Several electrochemically-active areas of microscopic dimensions, detected as brighter regions in the images, are randomly observed on the surface, most of the time with a quite regular disk shape ( $\varnothing \sim 20$ -30  $\mu$ m): the structure and dimensions of those sites can easily be correlated with the corresponding properties of pitting [corrosion] precursor sites observed on TiO<sub>2</sub>/Ti and Ta<sub>2</sub>O<sub>5</sub>/Ta surfaces [33-37,42,43]. All NiTi-based samples analyzed through this study evidence the random presence of those electroactive areas. The latter correspond to residual topographic imperfections on the underlying Nitinol

substrate, which are still randomly perceived. The impact of the blocking effect brought by the different surface modifications has thus to be carefully considered in this perspective. Indeed, the porous morphology of the Ta deposit implies a residual contact between the Nitinol defects and the external environment. Moreover, a further modification with C<sub>12</sub>P SAMs is not sufficient to allow for an exhaustive blocking of the residual reactive sites, even more with such moderate surface coverage ratios (~ 60%). A stronger hindering of the electrochemical response of the underlying Nitinol can be best achieved by depositing thicker and denser Ta<sub>2</sub>O<sub>5</sub> coatings that thus imply a strongly reduced (if not suppressed) porosity degree (work in progress).

Nevertheless, the beneficial supply of the complete surface treatment with both Ta and C<sub>12</sub>P in terms of imaging resolution is assessed when different  $E_{\text{substrate}}$  values are tested for the recording of SG/TC current maps, as already mentioned by Pust *et al.* who observed that the variation of the applied sample potential during the recording of a series of images resulted in contrast and homogeneity changes [40]. Electrochemically-active sites detected on SG/TC images of NiTi-Ta-C<sub>12</sub>P samples are perceptible throughout a wider range of  $E_{\text{substrate}}$  – -0.20 to -0.60 V/Ag-AgCl – and with a maximal resolution at  $E_{\text{substrate}} = E_p$  – here -0.44 V/Ag-AgCl (Fig. 9) –, while they are observed properly for the other substrates only at  $E_{\text{substrate}} \sim E_p$  (not shown).

The SG-TC mode of the SECM, in addition to considerably improve the imaging resolution compared to the FB mode, allows thus to monitor the electrochemical properties of the substrate. The latter may be directly stimulated by applying an appropriate potential directly to the substrate in order to reveal the presence of local areas more sensitive to corrosion. This  $E_{\text{substrate}}$  parameter is of great importance in further applied perspectives, notably in the biological field [68].

## 4. Conclusions

XPS, SEM, CV and SECM have been used for the characterization of NiTi substrates, pristine or covered with a tantalum electrodeposit and a 1-dodecylphosphonic acid monolayer. The effects of both Ta and C<sub>12</sub>P treatments, performed separately and additionally on NiTi, are evidenced by XPS measurements, showing good grafting efficiency and few contaminants. SEM imaging highlights the particular nanoporous morphology of the Ta layer. Meanwhile, CV analysis points out essential differences between surface modifications with Ta electrodeposits and C<sub>12</sub>P films regarding their blocking effect of the electron transfer with the redox mediator. NiTi plates covered with Ta layers, which intrinsically present nanopores all over their external surface, can be assimilated to blocking electrodes presenting “microscopic” (sub-micrometric) defects behaving as an array of interpenetrating (nano)electrodes. In contrast, the grafting of C<sub>12</sub>P leads to interfaces presenting “macroscopic” (supra-micrometric) defects. Covering rate values by Ta and C<sub>12</sub>P layers on

NiTi are calculated from both XPS and CV measurements and show globally good correspondence. Combination of both electrochemical and spectroscopic analysis suggests that both Ta and NiTi regions are covered equivalently by C<sub>12</sub>P moieties. Finally, a SECM study of the different samples through approach curves and current maps reveals their main electrochemical characteristics at a local scale. First-order heterogeneous finite kinetics fitted from experimental FB approach curves recorded for uncovered and covered NiTi surfaces highlight the differences in the regeneration of the mediator at these surfaces. SECM measurements specifically confirm that a more important blocking behavior is obtained when a combined modification by Ta and C<sub>12</sub>P is performed. Concerning the current maps, the FB mode does not lead to good-quality images resolution, probably because of the insufficient “fueling” of the mediator redox conversion in those conditions and settings. However, the polarization of the substrate through the SG-TC mode allows for the recording of better resolved images, with the exposure on all surfaces of several electrochemically-active areas of globally disk shape and micrometric dimensions, corresponding to residual pitting corrosion precursor sites on the underlying Nitinol substrates. The overall corrosion of the substrates and their precursor corrosion sites is reduced by introducing the inorganic and/or organic layers. However, these surface treatments, even combined, do not completely erase (or shadow) these corrosion precursor sites inherent to the pristine NiTi surface.

This work has provided many interesting data concerning the surface chemical composition, as well as on the global and local electrochemical characteristics of the substrates. Further surveys could make the connection with more applied biological perspectives. For instance, the study of the substrates behaviors at sample potential values of biological systems (~350-550 mV/SCE [68]) – and the resulting adaptation of experimental conditions (selection of redox probe, ...) – constitutes one possible interesting outlook, especially in terms of longer-term applied works (implant engineering, ...) where *in vitro* and *in vivo* investigations are involved.

## Acknowledgment

A.M. is grateful to FNRS-FRIA for Ph.D. student fellowship and funding for scientific mission in Paris.



## References

- [1] S.A. Shabalovskaya, On the nature of the biocompatibility and on medical applications of NiTi shape memory and superelastic alloys, *Biomed. Mater. Eng.* 1996, 6, 267.
- [2] S.A. Shabalovskaya, J. Anderegg, J. Van Humbeeck, Critical overview of Nitinol surfaces and their modifications for medical applications, *Acta Biomater.* 2008, 4, 447.
- [3] S.A. Shabalovskaya, G.C. Rondelli, A.L. Undisz, J.W. Anderegg, T.D. Burleigh, M.E. Rettenmayr, The electrochemical characteristics of native Nitinol surfaces, *Biomaterials* 2009, 30, 3662.
- [4] Z. Bai, H.H. Rotermund, The intrinsically high pitting corrosion resistance of mechanically polished Nitinol in simulated physiological solutions, *J. Biomed. Mater. Res. B* 2011, 99, 1.
- [5] J. Black, Biological performance of tantalum, *Clin. Mater.* 1994, 16, 167.
- [6] T. Miyazaki, H.-M. Kim, T. Kokubo, C. Ohtsuki, H. Kato, T. Nakamura, Mechanism of bonelike apatite formation on bioactive tantalum metal in a simulated body fluid, *Biomaterials* 2002, 23, 827.
- [7] B.R. Levine, S. Sporer, R.A. Poggie, C.J. Della Valle, J.J. Jacobs, Experimental and clinical performance of porous tantalum in orthopedic surgery, *Biomaterials* 2006, 27, 4671.
- [8] S. Zein El Abedin, U. Welz-Biermann, F. Endres, A study of the electrodeposition of tantalum on NiTi alloy in an ionic liquid and corrosion behaviour of the coated alloy, *Electrochem. Commun.* 2005, 7, 941.
- [9] C. Arnould, J. Delhalle, Z. Mekhalif, Multifunctional hybrid coating on titanium towards hydroxyapatite growth: Electrodeposition of tantalum and its molecular functionalization with organophosphonic acid films, *Electrochim. Acta* 2008, 53, 5632.
- [10] C. Arnould, J. Delhalle, Z. Mekhalif, Electrodeposition from ionic liquid of 2D ordered Ta<sub>2</sub>O<sub>5</sub> on titanium substrate through a polystyrene template, *J. Electrochem. Soc.* 2009, 156, K186.
- [11] A. Maho, J. Delhalle, Z. Mekhalif, Study of the formation process and the characteristics of tantalum layers electrodeposited on Nitinol plates in the 1-butyl-1-methylpyrrolidinium bis(trifluoromethylsulfonyl)imide ionic liquid, *Electrochim. Acta* 2013, 89, 346.

- [12] A. Maho, S. Linden, C. Arnould, S. Detriche, J. Delhalle, Z. Mekhalif, Tantalum oxide/carbon nanotubes composite coatings on titanium, and their functionalization with organophosphonic molecular films: a high quality scaffold for hydroxyapatite growth, *J. Colloid Interface Sci.* 2012, 371, 150.
- [13] B. Adolphi, E. Jahne, G. Busch, X. Cai, Characterization of the adsorption of x-(thiophene-3-yl alkyl) phosphonic acid on metal oxides with AR-XPS, *Anal. Bioanal. Chem.* 2004, 379, 646.
- [14] G. Mani, D.M. Johnson, D. Marton, V.L. Dougherty, M.D. Feldman, D. Patel, A.A. Ayon, C.M. Agrawal, Stability of self-assembled monolayers on titanium and gold, *Langmuir* 2008, 24, 6774.
- [15] B. Barthélémy, S. Devillers, I. Minet, J. Delhalle, Z. Mekhalif, Induction heating for surface triggering styrene polymerization on titanium modified with ATRP initiator, *J. Colloid Interface Sci.* 2011, 354, 873.
- [16] M. Maxisch, C. Ebbert, B. Torun, N. Fink, T. de los Arcos, J. Lackmann, H.J. Maier, G. Grundmeier, PM-IRRAS studies of the adsorption and stability of organophosphonate monolayers on passivated NiTi surfaces, *Appl. Surf. Sci.* 2011, 257, 2011.
- [17] Z. Petrovic, J. Katic, M. Metikos-Hukovic, H. Dadafarin, S. Omanovic, Modification of a Nitinol surface by phosphonate self-assembled monolayers, *J. Electrochem. Soc.* 2011, 158, F159.
- [18] L. Tan, R.A. Dodd, W.C. Crone, Corrosion and wear-corrosion behavior of NiTi modified by plasma source ion implantation, *Biomaterials* 2003, 24, 3931.
- [19] S. Shabalovskaya, G. Rondelli, J. Anderegg, J.P. Xiong, M. Wu, Comparative corrosion performance of black oxide, sandblasted, and fine-drawn Nitinol wires in potentiodynamic and potentiostatic tests: effects of chemical etching and electropolishing, *J. Biomed. Mater. Res. B* 2004, 69, 223.
- [20] F. Sun, K.N. Sank, J.L. Brash, I. Zhitomirsky, Surface modifications of Nitinol for biomedical applications, *Colloid. Surface. B* 2008, 67, 132.
- [21] R. Quinones, E.S. Gawalt, Polystyrene formation on monolayer-modified Nitinol effectively controls corrosion, *Langmuir* 2008, 24, 10858.
- [22] W. Simka, M. Kaczmarek, A. Baron-Wiechec, G. Nawrat, J. Marciniak, J. Zak, Electropolishing and passivation of NiTi shape memory alloy, *Electrochim. Acta* 2010, 55, 2437.
- [23] D. Qiu, L. Yang, Y. Yin, A. Wang, Preparation and characterization of hydroxyapatite/titania composite coating on NiTi alloy by electrochemical deposition, *Surf. Coat. Technol.* 2011, 205, 3280.

- [24] S. Devillers, B. Barthélémy, J. Delhalle, Z. Mekhalif, Induction heating vs conventional heating for the hydrothermal treatment of Nitinol and its subsequent 2-(methacryloyloxy)ethyl 2-(trimethylammonio)ethyl phosphate coating by surface-initiated atom transfer radical polymerization, *ACS Appl. Mater. Interfaces* 2011, 3, 4059.
- [25] I. Milosev, B. Kapun, The corrosion resistance of Nitinol alloy in simulated physiological solutions - Part 2: The effect of surface treatment, *Mater. Sci. Eng. C* 2012, 32, 1068.
- [26] I. Milosev, B. Kapun, The corrosion resistance of Nitinol alloy in simulated physiological solutions - Part 1: The effect of surface preparation, *Mater. Sci. Eng. C* 2012, 32, 1087.
- [27] A.J. Bard, M.V. Mirkin, *Scanning Electrochemical Microscopy*, Marcel Dekker Inc, New York, 2001.
- [28] G. Wittstock, M. Burchardt, S.E. Pust, Y. Shen, C. Zhao, Scanning electrochemical microscopy for direct imaging of reaction rates, *Angew. Chem. Int. Ed.* 2007, 46, 1584.
- [29] A. Kiani, M.A. Apluche-Aviles, P.K. Eggers, M. Jones, J.J. Gooding, M.N. Paddon-Row, A.J. Bard, Scanning electrochemical microscopy. 59. Effect of defects and structure on electron transfer through self-assembled monolayers, *Langmuir* 2008, 24, 2841.
- [30] A. Maho, J. Denayer, J. Delhalle, Z. Mekhalif, Electro-assisted assembly of aliphatic thiol, dithiol and dithiocarboxylic acid monolayers on copper, *Electrochim. Acta* 2011, 56, 3954.
- [31] H. Hazimeh, S. Nunige, R. Cornut, C. Lefrou, C. Combellas, F. Kanoufi, Surface reactivity from electrochemical lithography: illustration in the steady-state reductive etching of perfluorinated surfaces, *Anal. Chem.* 2011, 83, 6106.
- [32] T. Matrab, F. Hauquier, C. Combellas, F. Kanoufi, Scanning electron microscopy investigation of molecular transport and reactivity within polymer brushes, *ChemPhysChem* 2010, 11, 670.
- [33] N. Casillas, S.R. Snyder, W.H. Smyrl, H.S. White, Correlation of electron-transfer rates with the surface density of states of native and anodically grown oxide films on titanium, *J. Phys. Chem.* 1991, 95, 7002.
- [34] N. Casillas, S.J. Charlebois, W.H. Smyrl, H.S. White, Scanning electrochemical microscopy of precursor sites for pitting corrosion on titanium, *J. Electrochem. Soc.* 1993, 140, L142.

- [35] N. Casillas, S. Charlebois, W.H. Smyrl, H.S. White, Pitting corrosion of titanium, *J. Electrochem. Soc.* 1994, 141, 636.
- [36] S.B. Basame, H.S. White, Scanning electrochemical microscopy of native titanium oxide films. Mapping the potential dependence of spatially-localized electrochemical reactions, *J. Phys. Chem.* 1995, 99, 16430.
- [37] S.B. Basame, H.S. White, Scanning electrochemical microscopy: measurement of the current density at microscopic redox-active sites on titanium, *J. Phys. Chem. B* 1998, 102, 9812.
- [38] A. Schulte, S. Belger, M. Etienne, W. Schuhmann, Imaging localised corrosion of NiTi shape memory alloys by means of alternating current scanning electrochemical microscopy (AC-SECM), *Mater. Sci. Eng. A* 2004, 378, 523.
- [39] S.E. Pust, D. Scharnweber, C.N. Kirchner, G. Wittstock, Heterogeneous distribution of reactivity on metallic biomaterials: scanning probe microscopy studies of the biphasic Ti alloy Ti6Al4V, *Adv. Mater.* 2007, 19, 878.
- [40] S.E. Pust, D. Scharnweber, S. Baunack, G. Wittstock, Electron transfer kinetics at oxide films on metallic biomaterials, *J. Electrochem. Soc.* 2007, 154, C508.
- [41] R. Zhu, C. Nowierski, Z. Ding, J.J. Noël, D. Shosmith, Insights into grain structures and their reactivity on grade-2 Ti alloy surfaces by scanning electrochemical microscopy, *Chem. Mater.* 2007, 19, 2533.
- [42] S.B. Basame, H.S. White, Chemically-selective and spatially-localized redox activity at Ta/Ta<sub>2</sub>O<sub>5</sub> electrodes, *Langmuir* 1999, 15, 819.
- [43] S.B. Basame, H.S. White, Scanning electrochemical microscopy of metal/metal oxide electrodes. Analysis of spatially localized electron-transfer reactions during oxide growth, *Anal. Chem.* 1999, 71, 3166.
- [44] D.P. Wipf, Initiation and study of localized corrosion by scanning electrochemical microscopy, *Colloid. Surface. A* 1994, 93, 251.
- [45] A.M. Simoes, A.C. Bastos, M.G. Ferreira, Y. Gonzalez-Garcia, S. Gonzalez, R.M. Souto, Use of SVET and SECM to study the galvanic corrosion of an iron–zinc cell, *Corros. Sci.* 2007, 49, 726.
- [46] C.H. Paik, R.C. Alkire, Role of sulfide inclusions on localized corrosion of Ni200 in NaCl solutions, *J. Electrochem. Soc.* 2001, 148, B276.
- [47] M. Pahler, J.J. Santana, W. Schuhmann, R.M. Souto, Application of AC-SECM in corrosion science: local visualisation of inhibitor films on active metals for corrosion protection, *Chem. Eur. J.* 2011, 17, 905.

- [48] A.K. Neufeld, A.P. O'Mullane, Effect of the mediator in feedback mode-based SECM interrogation of indium tin-oxide and boron-doped diamond electrodes, *J. Solid State Electrochem.* 2006, 10, 806.
- [49] P.J. Cumpson, M.P. Seah, Elastic scattering corrections in AES and XPS. II. Estimating attenuation lengths and conditions required for their valid use in overlayer/substrate experiments, *Surf. Interface Anal.* 1997, 25, 430.
- [50] G. Chamoulaud, D. Bélanger, Spontaneous derivatization of a copper electrode with in situ generated diazonium cations in aprotic and aqueous media, *J. Phys. Chem. C* 2007, 111, 7501.
- [51] F. Hauquier, T. Matrab, F. Kanoufi, C. Combellas, Local direct and indirect reduction of electrografted aryldiazonium/gold surfaces for polymer brushes patterning, *Electrochim. Acta* 2009, 54, 5127.
- [52] C. Amatore, J.M. Savéant, D. Tessier, Charge transfer at partially blocked surfaces: a model for the case of microscopic active and inactive sites, *J. Electroanal. Chem.* 1983, 147, 39.
- [53] S.A. Shabalovskaya, J.W. Anderegg, Surface spectroscopic characterization of TiNi nearly equiatomic shape memory alloys for implants, *J. Vac. Sci. Technol. A* 1995, 13, 2624.
- [54] O. Kerrec, D. Devilliers, H. Groult, P. Marcus, Study of dry and electrogenerated Ta<sub>2</sub>O<sub>5</sub> and Ta:Ta<sub>2</sub>O<sub>5</sub>:Pt structures by XPS, *Mater. Sci. Eng. B* 1998, 55, 134.
- [55] L.P.H. Jeurgens, W.G. Sloof, F.D. Tichelaar, C.G. Borsboom, E.J. Mittemeijer, Determination of thickness and composition of aluminium-oxide overlayers on aluminium substrates, *Appl. Surf. Sci.* 1999, 144-145, 11.
- [56] M.-C. Bernard, A. Chaussé, E. Cabet-Deliry, M.M. Chemimi, J. Pinson, F. Podvorica, C. Vautrin-UI, Organic layers bonded to industrial, coinage, and noble metals through electrochemical reduction of aryldiazonium salts, *Chem. Mater.* 2003, 15, 3450.
- [57] G. Tanami, V. Gutkin, D. Mandler, Thin Nanocomposite Films of Polyaniline/Au Nanoparticles by the Langmuir-Blodgett Technique, *Langmuir* 2010, 26, 4239.
- [58] T.J. Davies, C.E. Banks, R.G. Compton, Voltammetry at spatially heterogeneous electrodes, *J. Solid State Electrochem.* 2005, 9, 797.
- [59] T. Gueshi, K. Tokuda, H. Matsuda, Voltammetry at partially covered electrodes. Part II. Linear potential sweep and cyclic voltammetry, *J. Electroanal. Chem.* 1979, 101, 29.

- [60] L. Forget, F. Wilwers, J. Delhalle, Z. Mekhalif, Surface modification of aluminum by n-pentane phosphonic acid: XPS and electrochemical evaluation, *Appl. Surf. Sci.* 2003, 205, 44.
- [61] D.M. Spori, N.V. Venkataraman, S.G.P. Tosatti, F. Durmaz, N.D. Spencer, S. Zürcher, Influence of alkyl chain length on phosphate self-assembled monolayers, *Langmuir* 2007, 23, 8053.
- [62] R. Quinones, E.S. Gawalt, Study of the formation of self-assembled monolayers on Nitinol, *Langmuir* 2007, 23, 10123.
- [63] G. Lecollinet, N. Delorme, M. Edely, A. Gibaud, J.-F. Bardeau, F. Hindré, F. Boury, D. Portet, Self-assembled monolayers of bisphosphonates: influence of side chain steric hindrance, *Langmuir* 2009, 25, 7828.
- [64] C. Wei, A.J. Bard, M.V. Mirkin, Scanning electrochemical microscopy. 31. Application of SECM to the study of charge transfer processes at the liquid/liquid interface, *J. Phys. Chem.* 1995, 99, 16033.
- [65] R. Cornut, C. Lefrou, New analytical approximation of feedback approach curves with a microdisk SECM tip and irreversible kinetic reaction at the substrate, *J. Electroanal. Chem.* 2008, 621, 178.
- [66] S. Nugues, G. Denuault, Scanning electrochemical microscopy: amperometric probing of diffusional ion fluxes through porous membranes and human dentine, *J. Electroanal. Chem.* 1996, 408, 125.
- [67] P. Roach, D. Eglin, K. Rohde, C.C. Perry, Modern biomaterials: a review—bulk properties and implications of surface modifications, *J. Mater. Sci.: Mater. Med.* 2007, 18, 1263.
- [68] D. Scharnweber, R. Beutner, S. Rössler, H. Worch, Electrochemical behavior of titanium-based materials - are there relations to biocompatibility? *J. Mater. Sci.: Mater. Med.* 2002, 13, 1215.

## Figures

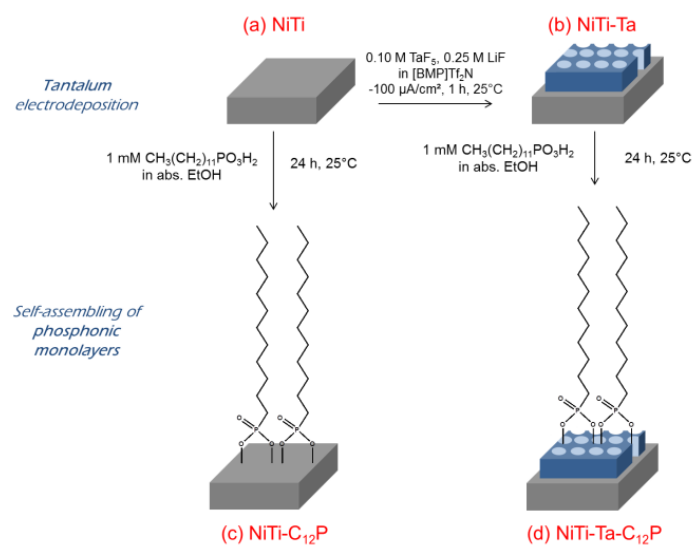


**Fig. 1.** Surface modification of NiTi (a) by tantalum electrodeposition (b), self-assembling of 1-dodecylphosphonic acid molecules (c), and both (d).

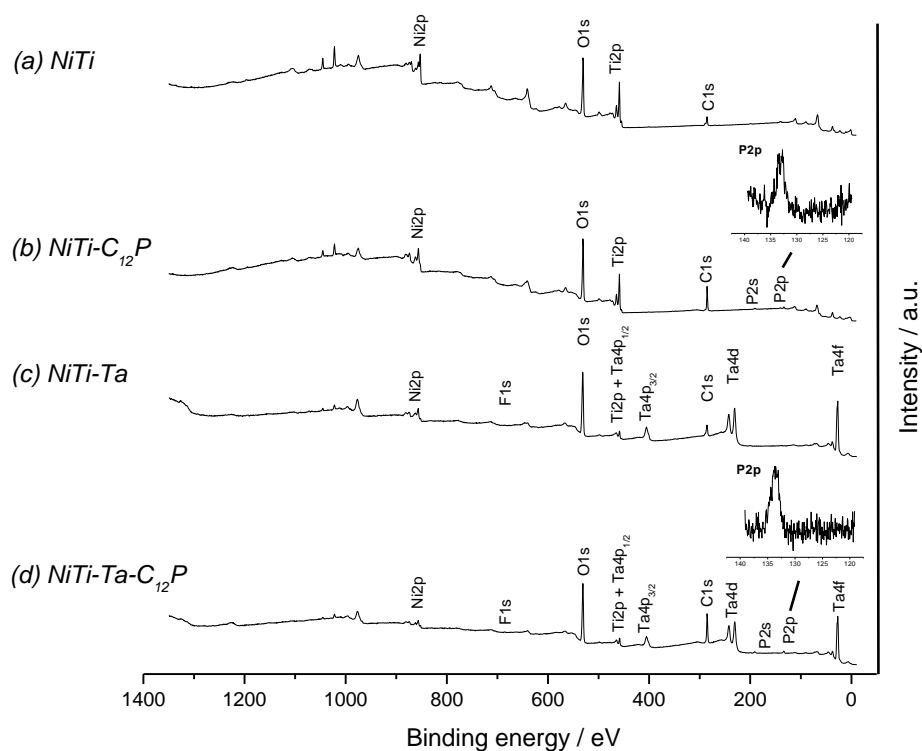


**Fig. 2.** XPS survey spectra of NiTi (a), NiTi-C<sub>12</sub>P (b), NiTi-Ta (c), and NiTi-Ta-C<sub>12</sub>P (d). Inserts: XPS core levels of P2p for NiTi-C<sub>12</sub>P (b) and NiTi-Ta-C<sub>12</sub>P (d).

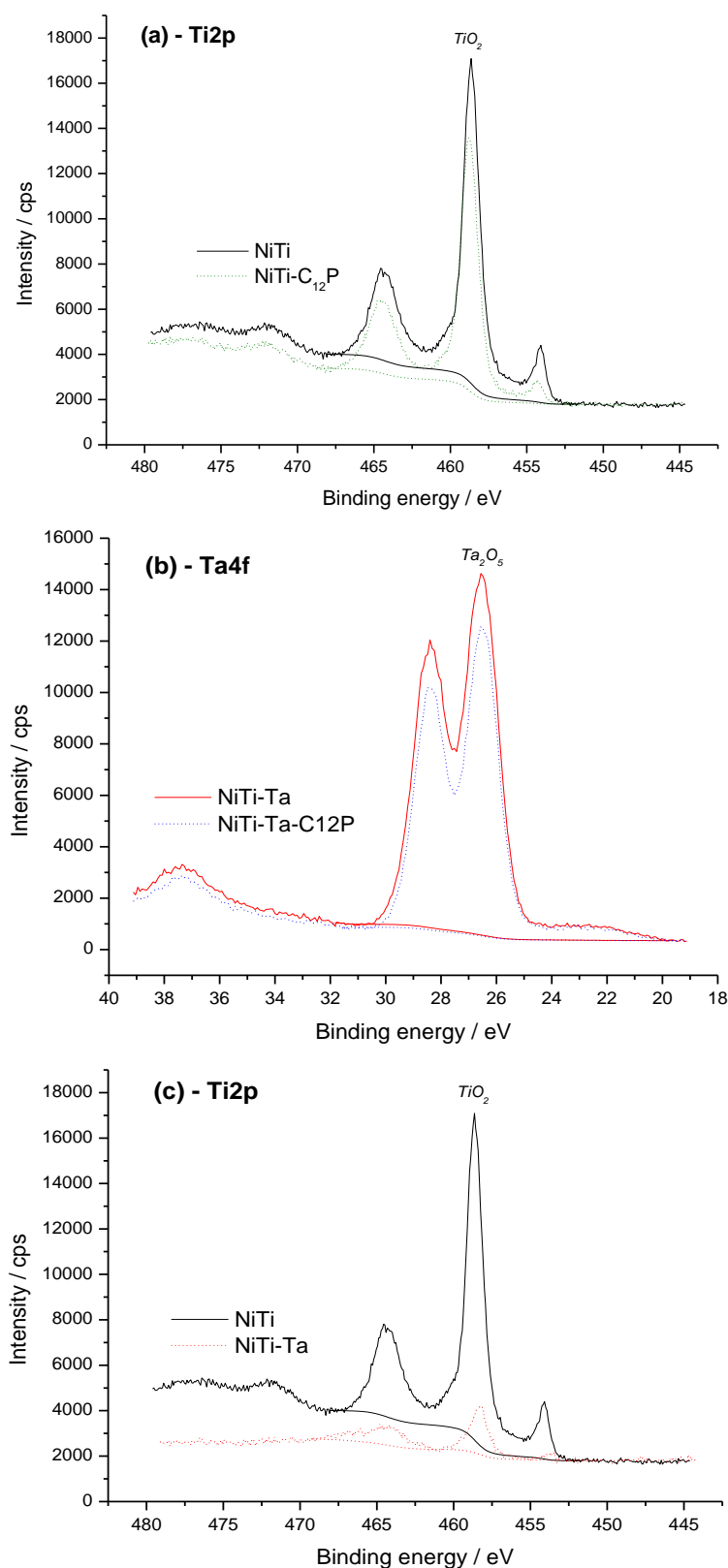


**Fig. 3.** XPS core levels of Ti2p for NiTi and NiTi-C<sub>12</sub>P (a), Ta4f for NiTi-Ta and NiTi-Ta-C<sub>12</sub>P (b), and Ti2p for NiTi and NiTi-Ta (c).



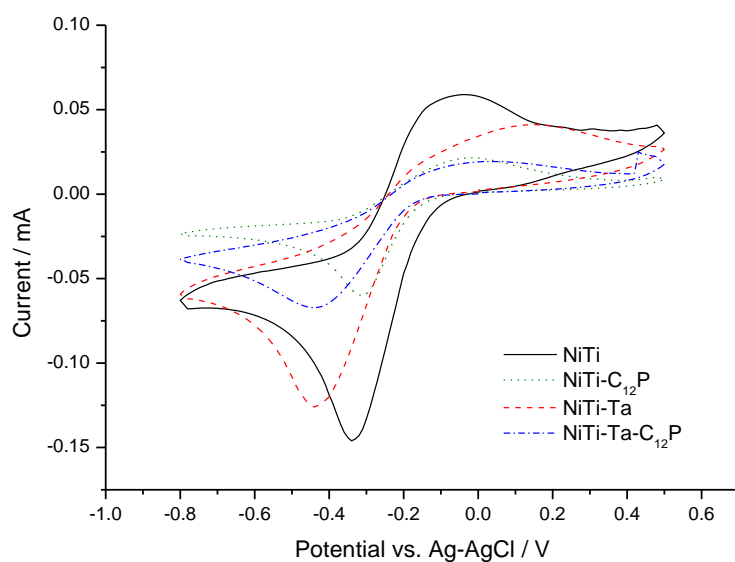


**Fig. 4.** Cyclic voltammetry curves for pristine NiTi (black), NiTi-C<sub>12</sub>P (green), NiTi-Ta (red) and NiTi-Ta-C<sub>12</sub>P (blue) samples in 5 mM Ru(NH<sub>3</sub>)<sub>6</sub>Cl<sub>3</sub> / 0.1 M K<sub>2</sub>SO<sub>4</sub> working solution at scan rate  $v = 20$  mV/s.

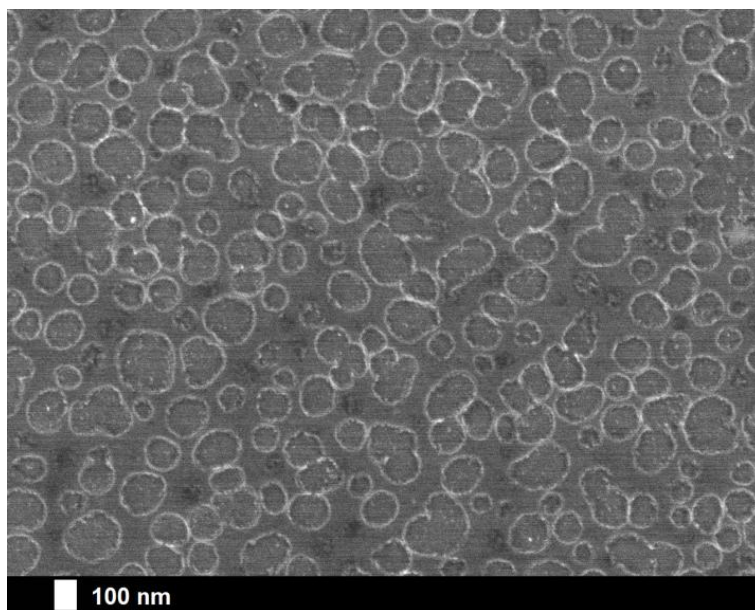


**Fig. 5.** SEM image of a NiTi-Ta surface.

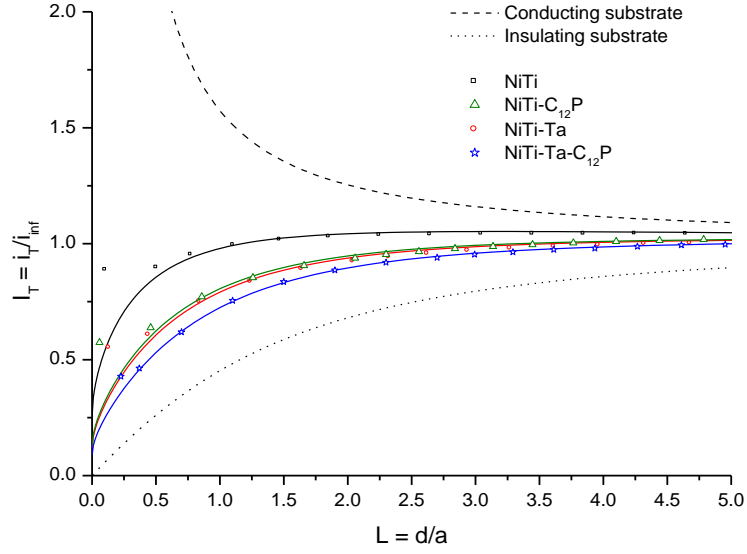


**Fig. 6.** Normalized SECM FB approach curves ( $v_z = 2 \mu\text{m/s}$ ,  $5 \text{ mM Ru(NH}_3)_6\text{Cl}_3 / 0.1 \text{ M K}_2\text{SO}_4$ ,  $E_{tip} = -0.70 \text{ V/Ag-AgCl}$ ,  $E_{substrate} = \text{OCP}$ ) measured for NiTi (black squares), NiTi-C<sub>12</sub>P (green triangles), NiTi-Ta (red circles) and NiTi-Ta-C<sub>12</sub>P (blue stars) samples. Solid lines are the theoretical curves for finite electron-transfer kinetics, while dashed and dotted lines are the theoretical curves for a conducting substrate and for a totally insulating substrate, respectively.

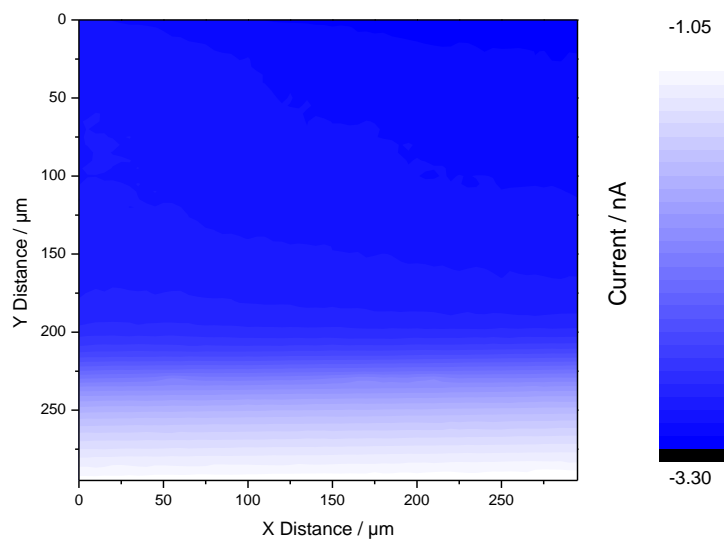


**Fig. 7.** SECM FB image ( $v_{x,y} = 25 \mu\text{m/s}$ ,  $5 \text{ mM Ru}(\text{NH}_3)_6\text{Cl}_3 / 0.1 \text{ M K}_2\text{SO}_4$ ) of a NiTi-Ta-C<sub>12</sub>P surface.  $E_{\text{tip}} = -0.70 \text{ V/Ag-AgCl}$ ,  $E_{\text{substrate}} = \text{OCP}$ .

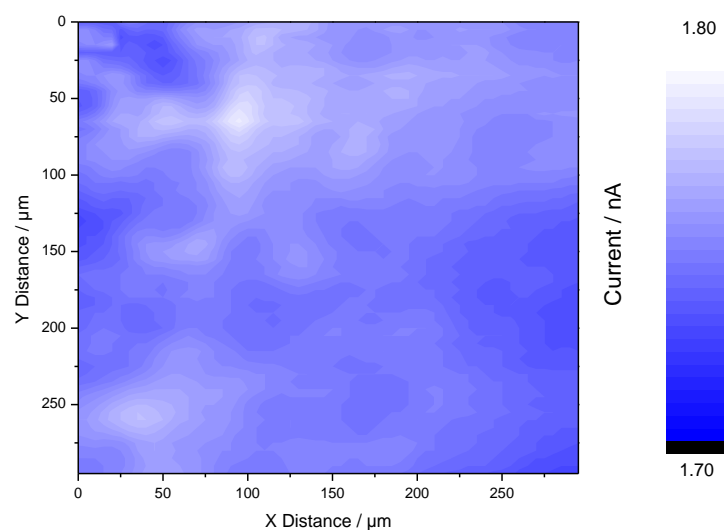


**Fig. 8.** SECM SG-TC image ( $v_{x,y} = 25 \mu\text{m/s}$ ,  $5 \text{ mM Ru}(\text{NH}_3)_6\text{Cl}_3 / 0.1 \text{ M K}_2\text{SO}_4$ ) of a NiTi-Ta-C<sub>12</sub>P surface.  $E_{\text{tip}} = +0.10 \text{ V/Ag-AgCl}$ ,  $E_{\text{substrate}} = -0.44 \text{ V/Ag-AgCl}$ . The x,y,z positions of the tip in Fig. 8 are the same as in Fig. 7.

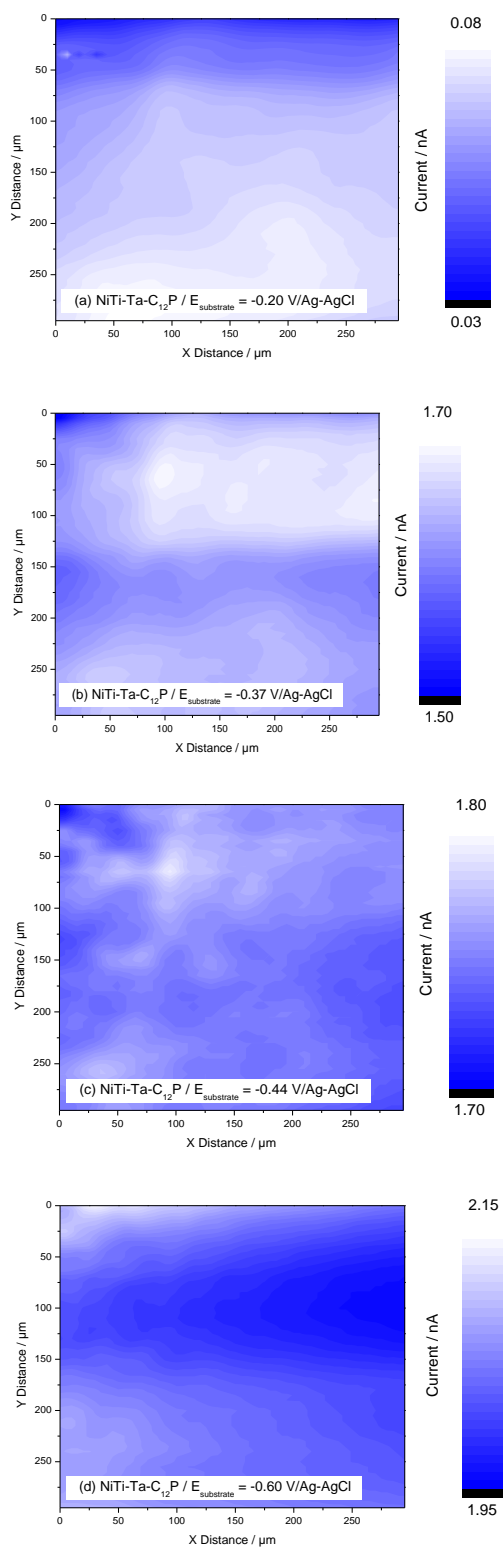


**Fig. 9.** SECM SG-TC images ( $v_{x,y} = 25 \mu\text{m/s}$ ,  $5 \text{ mM Ru}(\text{NH}_3)_6\text{Cl}_3 / 0.1 \text{ M K}_2\text{SO}_4$ ) of NiTi-Ta-C<sub>12</sub>P surfaces at  $E_{\text{substrate}} = -0.20 \text{ V/Ag-AgCl}$  (a),  $-0.37 \text{ V/Ag-AgCl}$  (b),  $-0.45 \text{ V/Ag-AgCl}$  (c), and  $-0.60 \text{ V/Ag-AgCl}$  (d).  $E_{\text{tip}} = +0.10 \text{ V/Ag-AgCl}$ . The  $x,y,z$  positions of the tip are the same in all images.

## Figure captions

**Fig. 1.** Surface modification of NiTi (a) by tantalum electrodeposition (b), self-assembling of 1-dodecylphosphonic acid molecules (c), and both (d).

**Fig. 2.** XPS survey spectra of NiTi (a), NiTi-C<sub>12</sub>P (b), NiTi-Ta (c), and NiTi-Ta-C<sub>12</sub>P (d). Inserts: XPS core levels of P2p for NiTi-C<sub>12</sub>P (b) and NiTi-Ta-C<sub>12</sub>P (d).

**Fig. 3.** XPS core levels of Ti2p for NiTi and NiTi-C<sub>12</sub>P (a), Ta4f for NiTi-Ta and NiTi-Ta-C<sub>12</sub>P (b), and Ti2p for NiTi and NiTi-Ta (c).

**Fig. 4.** Cyclic voltammetry curves for pristine NiTi (black), NiTi-C<sub>12</sub>P (green), NiTi-Ta (red) and NiTi-Ta-C<sub>12</sub>P (blue) samples in 5 mM Ru(NH<sub>3</sub>)<sub>6</sub>Cl<sub>3</sub> / 0.1 M K<sub>2</sub>SO<sub>4</sub> working solution at scan rate  $v = 20$  mV/s.

**Fig. 5.** SEM image of a NiTi-Ta surface.

**Fig. 6.** Normalized SECM FB approach curves ( $v_z = 2$   $\mu$ m/s, 5 mM Ru(NH<sub>3</sub>)<sub>6</sub>Cl<sub>3</sub> / 0.1 M K<sub>2</sub>SO<sub>4</sub>,  $E_{tip} = -0.70$  V/Ag-AgCl,  $E_{substrate} =$  OCP) measured for NiTi (black squares), NiTi-C<sub>12</sub>P (green triangles), NiTi-Ta (red circles) and NiTi-Ta-C<sub>12</sub>P (blue stars) samples. Solid lines are the theoretical curves for finite electron-transfer kinetics, while dashed and dotted lines are the theoretical curves for a conducting substrate and for a totally insulating substrate, respectively.

**Fig. 7.** SECM FB image ( $v_{x,y} = 25$   $\mu$ m/s, 5 mM Ru(NH<sub>3</sub>)<sub>6</sub>Cl<sub>3</sub> / 0.1 M K<sub>2</sub>SO<sub>4</sub>) of a NiTi-Ta-C<sub>12</sub>P surface.  $E_{tip} = -0.70$  V/Ag-AgCl,  $E_{substrate} =$  OCP.

**Fig. 8.** SECM SG-TC image ( $v_{x,y} = 25$   $\mu$ m/s, 5 mM Ru(NH<sub>3</sub>)<sub>6</sub>Cl<sub>3</sub> / 0.1 M K<sub>2</sub>SO<sub>4</sub>) of a NiTi-Ta-C<sub>12</sub>P surface.  $E_{tip} = +0.10$  V/Ag-AgCl,  $E_{substrate} = -0.44$  V/Ag-AgCl. The x,y,z positions of the tip in Fig. 8 are the same as in Fig. 7.

**Fig. 9.** SECM SG-TC images ( $v_{x,y} = 25$   $\mu$ m/s, 5 mM Ru(NH<sub>3</sub>)<sub>6</sub>Cl<sub>3</sub> / 0.1 M K<sub>2</sub>SO<sub>4</sub>) of NiTi-Ta-C<sub>12</sub>P surfaces at  $E_{substrate} = -0.20$  V/Ag-AgCl (a),  $-0.37$  V/Ag-AgCl (b),  $-0.45$  V/Ag-AgCl (c), and  $-0.60$  V/Ag-AgCl (d).  $E_{tip} = +0.10$  V/Ag-AgCl. The x,y,z positions of the tip are the same in all images.

## Tables

**Table 1.** XPS atomic percentages and ratios of pristine and modified NiTi samples.

Sample	C1s	O1s	Ni2p	Ti2p	P2p	Ta4f	F1s	C1s/P2p
	%	%	%	%	%	%	%	
NiTi	20	51	13	16	--	--	--	--
NiTi-C <sub>12</sub> P	32	44	10	11	3	--	--	13
NiTi-Ta	25	53	6	2	--	13	< 1	--
NiTi-Ta-C <sub>12</sub> P	41	41	3	2	3	10	< 1	14

**Table 2.** XPS peaks intensity, mean free path and layer thickness values for C<sub>12</sub>P and Ta films on NiTi.

Sample	Layer element A	Bulk element B	$I_B$	$I_{B,0}$	$\lambda_{B,A}$	$d_A$
			(cps)	(cps)	(nm)	(nm)
NiTi-C <sub>12</sub> P	C [C <sub>12</sub> P]	Ti [TiO <sub>2</sub> ]	11107.66	14012.67	3.4	0.79
NiTi-Ta-C <sub>12</sub> P	C [C <sub>12</sub> P]	Ta [Ta <sub>2</sub> O <sub>5</sub> ]	11936.13	14074.37	4.5	0.74
NiTi-Ta	Ta [Ta <sub>2</sub> O <sub>5</sub> ]	Ti [TiO <sub>2</sub> ]	2065.42	14012.67	1.1	2.1

**Table 3.** Cyclic voltammetry of pristine and modified NiTi samples.

Sample	$i_p^a$	$E_p^b$	$k_{app}^c$
	(mA)	(V/Ag-AgCl)	( $10^{-4}$ cm/s)
NiTi	-0.146	-0.34	3.1
NiTi-C <sub>12</sub> P	-0.060	-0.31	2.9
NiTi-Ta	-0.126	-0.45	0.92
NiTi-Ta-C <sub>12</sub> P	-0.067	-0.44	0.87

<sup>a</sup>Peak potential; <sup>b</sup>Peak current; <sup>c</sup>Apparent standard electron transfer rate constants  $k_{app}^{\circ}$  deduced from  $E_p$  and  $i_p$ .

**Table 4.** SECM of pristine and modified NiTi samples.

<b>Sample</b>	<b><math>k_{eff}^a</math> (<math>10^{-3}</math> cm/s)</b>
<b>NiTi</b>	4.6
<b>NiTi-C<sub>12</sub>P</b>	1.9
<b>NiTi-Ta</b>	1.7
<b>NiTi-Ta-C<sub>12</sub>P</b>	1.1

<sup>a</sup>First-order heterogeneous kinetic rate constants  $k_{eff}$  determined from SECM FB approach curves.